J. Mech. Phys. Solids 169 (2022) 105085

Contents lists available at ScienceDirect

Journal of the Mechanics and Physics of Solids

journal homepage: www.elsevier.com/locate/jmps

Supershear surface waves reveal prestress and anisotropy of soft materials

Guo-Yang Li *, Xu Feng, Antoine Ramier, Seok-Hyun Yun *

Harvard Medical School and Wellman Center for Photomedicine, Massachusetts General Hospital, Boston, MA 02139, USA

ARTICLE INFO

Keywords:
Surface wave
Leaky wave
Acoustoelasticity
Anisotropic elasticity
Optical coherence elastography

ABSTRACT

Surface waves play important roles in many fundamental and applied areas from seismic detection to material characterizations. Supershear surface waves with propagation speeds greater than bulk shear waves have recently been reported, but their properties are not well understood. Here we describe theoretical and experimental results on supershear surface waves in rubbery materials. We find that supershear surface waves can be supported in viscoelastic materials with no restriction on the shear quality factor. Interestingly, the effect of prestress on the speed of the supershear surface wave is opposite to that of the Rayleigh surface wave. Furthermore, anisotropy of material affects the supershear wave much more strongly than the Rayleigh surface wave. We offer heuristic interpretation as well as theoretical verification of our experimental observations. Our work points to the potential applications of supershear waves for characterizing the bulk mechanical properties of soft solid from the free surface.

1. Introduction

Surface wave motion in solids is a classical problem in mechanics, acoustics and seismology, and has found broad applications in nondestructive testing (NDT) of materials (Herrmann et al., 2006; Garnier et al., 2013; Walker et al., 2012), surface acoustic wave devices (Friend and Yeo, 2011; Ozcelik et al., 2018; Munk et al., 2019) and seismic activity monitoring (Debayle et al., 2020; Levshin et al., 2018; Gao et al., 2014). The Rayleigh (R) surface wave is the most well studied wave propagating on the free surface of solid. Besides the R wave, another type of surface wave that travels with a greater speed than the bulk shear waves have been observed on the free surface of a solid (Le Goff et al., 2013; Pitre et al., 2019). This so-called supershear (SS) surface wave (or supershear evanescent wave, SEW, see for example Pitre et al., 2019) allows the surface elastic energy to propagate away with a greater speed and is likely responsible for the supershear dynamics at the surface, such as the supershear crack propagation and supershear earthquake (Bhat et al., 2007; Das, 2007; Passelègue et al., 2013; Socquet et al., 2019). Besides the free surface, a very recent study by Nguyen et al. (2022) suggest the SEW can also be supported at the soft solid–fluid interface.

Recently, growing needs for mechanical characterization of soft matters, such as elastomers, hydrogels and biological tissues, have spurred renewed interests in surface wave motion (Li et al., 2018; Nam et al., 2016; Rudykh and Boyce, 2014; Pitre et al., 2019; Zhang and Greenleaf, 2007; Ramier et al., 2019; Dong et al., 2020; Norris and Parnell, 2012). While the R wave in soft matters is well established and explored for applications, much less is known about SS surface waves (Pitre et al., 2019). SS surface waves are inherently leaky in order to manifest a higher speed than bulk shear waves. While SS surface waves in elastic solids have been described (Schröder and Scott, 2001), some studies (Carcione, 2007; Le Goff et al., 2013) claimed that SS surface waves can only be supported when the shear wave quality factor (i.e., storage modulus/loss modulus) is less than 6.29, and there has been a debate whether SS surface waves is supported in viscoelastic materials with weak attenuation.

* Corresponding authors.
E-mail addresses: gli26@mgh.harvard.edu (G.-Y. Li), syun@hms.harvard.edu (S.-H. Yun).

https://doi.org/10.1016/j.jmps.2022.105085
Received 17 April 2022; Received in revised form 19 August 2022; Accepted 22 September 2022
Available online 1 October 2022
0022-5096/

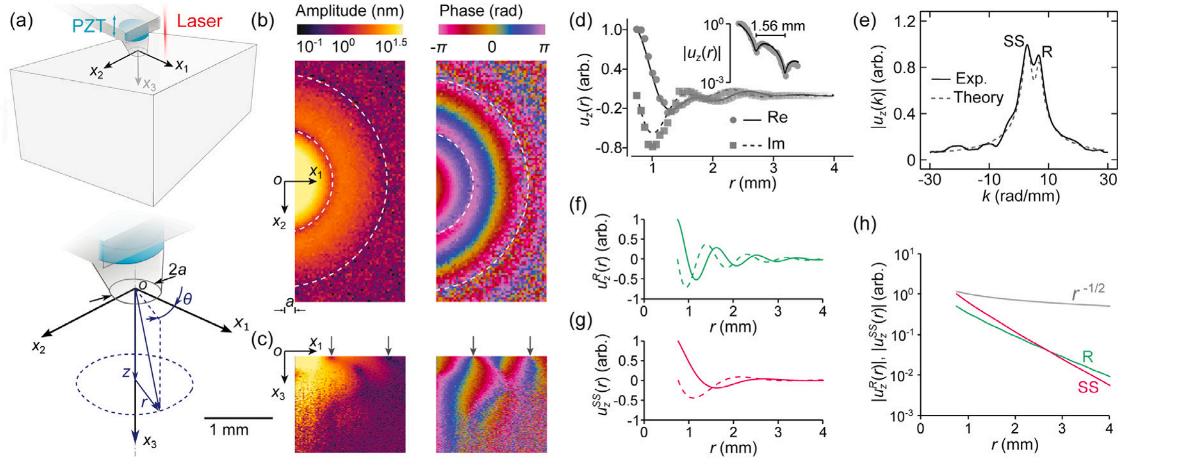

Fig. 1. Experimental observation of SS waves in an elastomer. (a) Experimental setup. (b) and (c) The amplitude and phase maps of the top surface and the cross-section. The arrows and dashed lines indicate nodes of destructive interference between the SS and R waves.(d) A comparison of the experiment ($f_s = 12$ kHz) and the theoretical model for the surface displacement. Markers, experiment; lines, theory. Inset: the total wave amplitude. (e) A comparison in the wavenumber domain. (f) and (g) Surface displacements of the R and SS waves calculated from the theoretical model. Solid and dashed lines denote the real and imagery parts, respectively. (h) Amplitudes of the R and SS waves.

Another aspect of the SS surface waves that remains unexplored is how the anisotropy of the solid affects the speeds of the SS surface waves. The theory of surface waves in anisotropic elastic materials has been well established owing to the early contributions to this field (Farnell, 1970; Stroh, 1962, 1958; Barnett and Lothe, 1985; Biryukov, 1985; Fu and Mielke, 2002). A summary of the work can be found in the review paper by Chadwick and Smith (1977). Notably, the theoretical work by Farnell (1970) successfully explains the experimental observation of the pseudo surface waves. Pseudo surface waves can arise near the [110] direction, on the (001) plane of the cubic crystals. Along these directions, two shear waves exist; the one with a polarization direction lying in the (001) plane has a lower speed (denoted by T2) than the one with a polarization direction perpendicular to the (001) plane (denoted by T1). The speed of the Rayleigh surface is lower than the two shear waves, whereas the pseudo surface wave has a greater speed than T2 but lower than T1. The greater speed makes the pseudo surface wave a leaky mode. However, the attenuation of the pseudo surface is rather weak due to its weak coupling with T2. The SS surface wave has a speed greater than the two shear waves, which usually results in a far stronger attenuation due to the coupling with T1. The strong attenuation implies that the SS surface waves can only be observed in the near field (evanescent field), which is likely the reason why the SS surface waves have been overlooked in crystals.

In this study, we reveal several underappreciated properties of SS waves in soft materials via experimental and theoretical investigations. Firstly, we show the SS waves can be supported over a broad frequency range, with no restriction on dissipation of the material. Secondly, we show that the compressive/tensile stress on the soft material increases/decreases the speed of the SS wave, which is opposite to what is commonly known for R wave. We account for this interesting result using the acoustoelastic theory, finite-element (FE) simulation, and simple heuristic explanation. Extending this finding, we show how material anisotropy affects SS waves distinctly different from R waves.

2. Experimental observation of supershear surface wave using optical coherence tomography

To demonstrate the SS waves in soft materials, we built the experimental setup depicted in Fig. 1(a) using a home-built optical coherence tomography (OCT) (Ramier et al., 2019). The sample is a silicone rubber Ecoflex 0050, Smooth-On Inc., with mass density $\rho \approx 1070\ \mathrm{kg/m^3}$ and refractive index $n \approx 1.4$. The approximate size is $8 \times 4\ \mathrm{cm}^2$ in the lateral extent and 4 cm along depth, which is large enough to avoid wave reflections at the edges. Mechanical waves were excited by a vertically vibrating, flat tip with a circular contact area with a radius a of ~ 0.75 mm, which is driven by a PZT actuator. The driving frequency of the PZT, f_s, can be tuned from 100 Hz to 20 kHz. To measure the wave propagation, we operated the OCT with a M-B scan mode (Ramier et al., 2019). In brief, when the probe started to vibrate, the laser beam was triggered to continuously scan 350 times at a location (M scan), with a acquisition rate of ~43.2 kHz. Then the laser beam was moved to another location by a galvanometer scan mirror, and the M scan were repeated (B Scan). The displacement measured from each M scan was Fourier transformed to obtain the real and imagery parts of the displacement.

Fig. 1(b)–(c) show a representative wave field measured when $f_s = 12$ kHz. The minimums in wave amplitude and fluctuations in phase (indicated by dashed lines and arrows in Fig. 1(b)–(c)) represent destructive interference between the R and SS waves. The two wave modes can be resolved in wavenumber domain. By performing the Fourier transformation to the radical surface displacement shown in Fig. 1(d), we move the data from the spatial domain to the wavenumber domain, where two peaks that correspond to the R and SS waves, respectively, can be identified (see Fig. 1(e)). This experimental observation clearly suggests the R and SS waves are two predominant surface wave modes in the near-field.

3. Mechanical model for surface wave excitation

To understand the experiment, we perform a theoretical study on the surface waves and obtain an analytical solution for the near-field surface displacement. Consider a semi-finite solid which occupies the space $z \geq 0$, as shown in Fig. 1(a). Since the problem is axisymmetric, we introduce a cylindrical coordinate system (r, θ, z) and suppose the tip imposes a uniform time-harmonic pressure $p(r,t) = p_0 e^{i\omega t}$ $(r \leq a)$ to the contact surface, where p_0 denotes the amplitude of the pressure, a is the radius of the cylindrical tip, t is the time, and $\omega = 2\pi f_s$. The time-harmonic stimulus results in the displacement $\boldsymbol{u} = \boldsymbol{u}_0 e^{i\omega t}$, where $\boldsymbol{u}_0 = u_{0r}\boldsymbol{e}_r + u_{0z}\boldsymbol{e}_z$. $\mathbf{e}_r$ and $\mathbf{e}_z$ denote the unit vectors along r and θ directions, respectively. Inserting $\boldsymbol{u}$ into the equation of motion $(\lambda+2\mu)\nabla\nabla\cdot\boldsymbol{u} - \mu\nabla\times\nabla\times\boldsymbol{u} = \rho\partial^2\boldsymbol{u}/\partial t^2$, we get

$$(\lambda + 2\mu)\nabla\nabla \cdot \boldsymbol{u}_0 - \mu\nabla \times \nabla \times \boldsymbol{u}_0 = -\rho\omega^2\boldsymbol{u}_0, \tag{1}$$

where ρ is the density. λ and μ are Lamé constants and $\lambda \gg \mu$ for soft solids studied here.

To solve this problem, we introduce $\phi = \nabla \cdot \boldsymbol{u}_0$ and $\psi\boldsymbol{e}_\theta = \nabla \times \boldsymbol{u}_0$, where $\boldsymbol{e}_\theta$ denotes the unit vector along θ direction.

$$\phi = \frac{1}{r}\frac{\partial(ru_{0r})}{\partial r} + \frac{\partial u_{0z}}{\partial z}, \quad \psi = \frac{\partial u_{0r}}{\partial z} - \frac{\partial u_{0z}}{\partial r}. \tag{2}$$

Inserting Eq. (2) into Eq. (1) we get

$$(\lambda + 2\mu)\frac{\partial\phi}{\partial z} - \frac{\mu}{r}\frac{\partial(r\psi)}{\partial r} + \rho\omega^2 u_{0z} = 0, \quad (\lambda + 2\mu)\frac{\partial\phi}{\partial r} + \mu\frac{\partial\psi}{\partial z} + \rho\omega^2 u_{0r} = 0. \tag{3}$$

Eliminating ϕ and ψ from Eq. (3) yields following decoupled equilibrium equations

$$\frac{1}{r}\frac{\partial}{\partial r}\left(r\frac{\partial\phi}{\partial r}\right) + \frac{\partial^2\phi}{\partial z^2} + k_L^2\phi = 0, \quad \frac{\partial}{\partial r}\left[\frac{1}{r}\frac{\partial}{\partial r}(r\psi)\right] + \frac{\partial^2\psi}{\partial z^2} + k_S^2\psi = 0, \tag{4}$$

where $k_L = \omega/\sqrt{(\lambda + 2\mu)/\rho}$ and $k_S = \omega/\sqrt{\mu/\rho}$.

The in-plane components of the Cauchy stress $\boldsymbol{\sigma}$, expressed in terms of ϕ and ψ, are (neglecting the time harmonic terms)

$$\begin{aligned}\frac{\rho\omega^2}{\mu^2}\sigma_{zz} &= \frac{2}{r}\frac{\partial}{\partial r}\left(r\frac{\partial\psi}{\partial z}\right) - \frac{v^2(v^2-2)}{r}\frac{\partial}{\partial r}\left(r\frac{\partial\phi}{\partial r}\right) - v^4\frac{\partial^2\phi}{\partial z^2}, \\ \frac{\rho\omega^2}{\mu^2}\sigma_{zr} &= \frac{\partial}{\partial r}\left[\frac{1}{r}\frac{\partial(r\psi)}{\partial r}\right] - \frac{\partial^2\psi}{\partial z^2} - 2v^2\frac{\partial^2\phi}{\partial r\partial z},\end{aligned} \tag{5}$$

where $v = k_S/k_L$. The boundary conditions on the free surface are

$$\sigma_{zz} = p_0(r \leq a), \quad \sigma_{zz} = 0(r > a), \quad \sigma_{zr} = 0, \tag{6}$$

where we again neglect the time harmonic terms. Inserting Eq. (6) into Eq. (5) we thus get the boundary conditions expressed in terms of ϕ and ψ.

To solve Eq. (4), here we follow the Miller's work (Miller et al., 1954) and perform Hankel transformation to Eq. (4) (from r to k)

$$\frac{\mathrm{d}^2\bar{\phi}_0}{\mathrm{d}z^2} - (k^2 - k_L^2)\bar{\phi}_0 = 0, \quad \frac{\mathrm{d}^2\bar{\psi}_1}{\mathrm{d}z^2} - (k^2 - k_S^2)\bar{\psi}_1 = 0, \tag{7}$$

where $\bar{\phi}_0$ and $\bar{\psi}_1$ are the 0 and 1-order Hankel transformations of ϕ and ψ, i.e.,

$$\bar{\phi}_0(k,z) = \int_0^\infty \phi(r,z)rJ_0(kr)\mathrm{d}r, \quad \bar{\psi}_1(k,z) = \int_0^\infty \psi(r,z)rJ_1(kr)\mathrm{d}r, \tag{8}$$

where J_0 and J_1 are the Bessel function of the first kind of order 0 and 1, respectively. Similarly, we perform Hankel transformations of Eqs. (5) and (6) to get

$$\frac{\rho\omega^2}{\mu^2}\bar{\sigma}_{zz,0} = -v^4\frac{\partial^2\bar{\phi}_0}{\partial z^2} + 2k\frac{\mathrm{d}\bar{\psi}_1}{\mathrm{d}z} + v^2(v^2-2)k^2\bar{\phi}_0, \quad \frac{\rho\omega^2}{\mu^2}\bar{\sigma}_{zr,1} = -\left(\frac{\mathrm{d}^2\bar{\psi}_1}{\mathrm{d}z^2} - 2v^2k\frac{\mathrm{d}\bar{\phi}_0}{\mathrm{d}z} + k^2\bar{\psi}_1\right), \tag{9}$$

and

$$\bar{\sigma}_{zz,0} = \frac{ap_0J_1(ka)}{k}, \quad \bar{\sigma}_{zr,1} = 0, \tag{10}$$

where $\bar{\sigma}_{zz,0}$ and $\bar{\sigma}_{zr,1}$ are the 0 and 1-order Hankel transformations of σ_{zz} and σ_{zr}, respectively.

Solving Eq. (7) with the boundary conditions given by Eqs. (9) and (10), we get

$$\bar{\phi}_0 = \frac{\rho\omega^2(k_S^2 - 2k^2)}{v^2\mu^2 k\mathcal{F}(k)}ap_0J_1(ka)e^{-z\sqrt{k^2-k_L^2}}, \quad \bar{\psi}_1 = \frac{2\rho\omega^2\sqrt{k^2-k_L^2}}{\mu\mathcal{F}(k)}aJ_1(ka)e^{-z\sqrt{k^2-k_S^2}}, \tag{11}$$

where

$$\mathcal{F}(k) = (2k^2 - k_S^2)^2 - 4k^2\sqrt{k^2-k_L^2}\sqrt{k^2-k_S^2}. \tag{12}$$

It should be noted that in Eq. (11), we have taken $e^{-z\sqrt{k^2-k_S^2}}$ for $\bar{\psi}_1$ to make sure $\bar{\psi}_1 \to 0$ when $z \to +\infty$. For SS wave, however, we should take $e^{z\sqrt{k^2-k_S^2}}$ for $\bar{\psi}_1$ to manifest the leaky nature of the SS wave (see discussions on the nature of a leaky wave mode in, for example, Refs. Farnell (1970) and Xu and Wu (2013)). This choice results in a plus sign for the second term of $\mathcal{F}(k)$. To get a universal form for the secular equation, we replace the Eq. (12) with

$$\mathcal{F}(k) = (2k^2 - k_S^2)^2 - 4k^2\sqrt{k^2 - k_L^2}\sqrt{k^2 - k_S^2} \cdot \mathrm{sign}\{\mathrm{Re}(k^2 - k_S^2)\}. \tag{13}$$

Inserting Eq. (11) into the Hankel transformation of Eq. (2), we get the Hankel transformations of u_{0z} and u_{0r}, denoted by $\bar{u}_{z,0}$ and $\bar{u}_{r,1}$, are

$$\begin{aligned} \bar{u}_{z,0} &= \frac{ap_0 J_1(ka)\sqrt{k^2 - k_L^2}}{\mu k \mathcal{F}(k)}\left[2k^2 e^{-z\sqrt{k^2-k_S^2}} + (k_S^2 - 2k^2)e^{-z\sqrt{k^2-k_L^2}}\right], \\ \bar{u}_{r,1} &= \frac{ap_0 J_1(ka)}{\mu \mathcal{F}(k)}\left[2\sqrt{k^2 - k_L^2}\sqrt{k^2 - k_S^2}e^{-z\sqrt{k^2-k_S^2}} + (k_S^2 - 2k^2)e^{-z\sqrt{k^2-k_L^2}}\right]. \end{aligned} \tag{14}$$

The displacements u_{0z} and u_{0r} can be obtained by performing inverse Hankel transformations to Eq. (14). Here we focus on the vertical displacement u_{0z}, which can be measured using our experimental setup. From the inverse Hankel transformation of $\bar{u}_{z,0}$ we get

$$u_{0z}(r,z) = \frac{ap_0}{\mu}\int_0^{\infty} \frac{J_1(ka)\sqrt{k^2 - k_L^2}}{\mathcal{F}(k)}\left[2k^2 e^{-z\sqrt{k^2-k_S^2}} + (k_S^2 - 2k^2)e^{-z\sqrt{k^2-k_L^2}}\right] J_0(kr)\mathrm{d}k. \tag{15}$$

According to Royston et al. (1999), an equivalent form of Eq. (15) is

$$u_{0z}(r,z) = \frac{ap_0 i}{\pi\mu}\int_{-\infty}^{\infty} \frac{J_1(ka)\sqrt{k^2 - k_L^2}}{\mathcal{F}(k)}\left[2k^2 e^{-z\sqrt{k^2-k_S^2}} + (k_S^2 - 2k^2)e^{-z\sqrt{k^2-k_L^2}}\right] K_0(-ikr)\mathrm{d}k, \tag{16}$$

where K_0 is the modified Bessel function of the second kind. The superiority of Eq. (16) is that the Cauchy principal value theorem is applicable. There are some comprehensive discussions on how to deal with the contributions from the poles and the branch cuts (Graff, 1991; Harris and Achenbach, 2002; Schröder and Scott, 2001) when performing the integration in Eq. (16). Since we are only interested in the surface waves, we can neglect the contributions of the branch integrals and only consider the contributions of the residues (Graff, 1991). Therefore, we get

$$u_z(r,0) = \frac{2ap_0 k_S^2}{\mu}\sum_k \frac{J_1(ka)\sqrt{k^2 - k_L^2}}{\mathcal{F}'(k)} K_0(ikr), \tag{17}$$

where $\mathcal{F}' = \partial\mathcal{F}/\partial k$, and k denotes the root of $\mathcal{F}(k) = 0$.

For soft materials with $\lambda \gg \mu$, we have $k, k_S \gg k_L$. In this case Eq. (13) reduce to

$$\mathcal{F}(k) = (2k^2 - k_S^2)^2 - 4k^2\sqrt{k^2(k^2 - k_S^2)} \cdot \mathrm{sign}\{\mathrm{Re}(k^2 - k_S^2)\}. \tag{18}$$

Two roots of Eq. (18) that correspond to the Rayleigh and supershear surface waves, respective, are $k_R = 1.047k_S$ and

$$k_{SS} = (0.4696 - 0.1355i)k_S. \tag{19}$$

The other root of Eq. (18), however, has a positive imagery part, which denotes an exponential increase in wave amplitude along the radial direction. This root is physically unrealistic thus is excluded (Schröder and Scott, 2001).

Inserting k_R and k_{SS} into Eq. (17) we get

$$u_{0z}(r) = i\pi\frac{ap_0 k_S^2}{\mu}\left[\frac{J_1(k_R a)k_R}{\mathcal{F}'(k_R)}H_0^{(1)}(-k_R r) + \frac{J_1(k_{SS}a)k_{SS}}{\mathcal{F}'(k_{SS})}H_0^{(1)}(-k_{SS}r)\right] = u_z^R(r) + u_z^{SS}(r), \tag{20}$$

where we have used the Hankel function of the first kind $H_0^{(1)}(x)$ to take the place of $K_0(x)$ (note that $K_0(x) = i\pi/2H_0^{(1)}(ix)$). For large r, $H_0^{(1)}(-kr) \to e^{-ikr}r^{-1/2}$; Eq. (20) describes the two propagating waves with wavenumbers, k_R and k_{SS}.

The phase velocity c of a wave is related to its wavenumber k, via $c = 2\pi f_s/\mathrm{Re}(k)$. For elastic materials with a real value of k_S, according to Eq. (19) the SS wave is leaky with a complex value of k_{SS}, and $c_{SS} = 2.13c_{T0}$, where $c_{T0} = \sqrt{\mu/\rho}$ is the shear wave speed. For viscoelastic materials, we find c_{SS}/c_{T0} increases slightly as the shear quality factor Q, which is defined as

$$Q = \mathrm{Re}(\mu)/\mathrm{Im}(\mu), \tag{21}$$

decreases; for example, it is 2.18 at $Q = 6$ and 2.99 at $Q = 0$.

The two terms in Eq. (20) result in the interference patterns observed in our experiments. To quantitatively compare the theoretical model and experiments, in Fig. 1(d) we show the experimental displacements (markers) along the radial direction at $f_s = 12$ kHz and the theoretical curves obtained by fitting the data with Eq. (20) with k_S as the only fitting parameter. The best fitting gives the storage modulus $\mu' = 110.8 \pm 2.2$ kPa and the loss modulus $\mu'' = 33.7 \pm 2.9$ kPa ($\mu = \mu' + i\mu''$). By performing the Fourier transformation we move the data from the spatial domain to the wavenumber domain (see Fig. 1(e)) and observe two peaks that correspond to the R and SS waves, respectively. The theoretical model shows a good agreement with the experiment in the wavenumber domain. Strictly speaking, an inverse Hankel transformation is required to extract the wavenumber from the displacement profiles. However, we find that the Fourier transformation is a convenient approximation with errors less than 4% for all our experimental cases.

In Fig. 1(f) and (g) we plot $u_z^R(r)$ and $u_z^{SS}(r)$, respectively. As shown in Fig. 1(h), the wave amplitudes decrease exponentially over r, much steeper than the $r^{-1/2}$ dependence expected for radially propagating surface waves in pure elastic materials (Rose, 2014). The fast exponential decay is due to the viscoelasticity of the sample. The decay rate of SS and Rayleigh surface waves can be comparable, highlighting the essential role of the SS surface wave in soft materials, especially in the high-frequency regime.

4. Supershear surface wave is supported in incompressible materials with no restriction on the shear quality factor Q

The existence of the SS waves has been debated. Some studies claimed that the SS waves can only exist when $Q < 6.29$ (see discussions on page 146 of Carcione (2007)). This claim is supported by a recent experimental study, in which the SS waves were observed when $Q \approx 1.32$ (Le Goff et al., 2013). However, another theoretical study predicts the existence of the SS waves in elastic materials (Q is infinite) with Poisson's ratios greater than 0.26 (Schröder and Scott, 2001). Since the Poisson's ratios for soft materials interested in present study are close to 0.5, the claim given by Schröder and Scott (2001) seems to indicate that SS waves are supported with no restriction on the shear quality factor Q. To address this debate we further studied the effect of viscoelasticity on SS waves.

For the rubber sample we varied the stimulus frequency from 100 Hz to 20 kHz. Fig. 2(a) and (b) show the surface displacements obtained at f_s from 2 kHz to 20 kHz in the spatial and wavenumber domains, which quantitatively agree with our theoretical predictions (see the comparison in Fig. 3). The relative amplitudes of the two modes are frequency dependent because the excitation efficiencies of the waves are sensitive to the ratios between the wavelengths and the size, a, of pressure loading. From Eq. (20), for $a = 0.75$ mm we find that $|u_z^{SS}(a)| > |u_z^R(a)|$ when $f_s > 5$ kHz, indicating the SS wave is primarily excited at high frequency regime. This result explains the previous experimental observation where the SS waves become dominant if applying a high-speed impact to the surface (Le Goff et al., 2013). In the low frequency regime, only the R wave can be robustly measured (100 Hz to 1 kHz, see the gray markers in Fig. 2(c)) likely because the lateral scan length of our OCT system is too short to capture the SS waves.

From the measured wavenumbers, the phase velocities are computed, as shown in Fig. 2(c) and (d). By fitting the broad band dispersion relation (100 Hz to 20 kHz), we find the viscoelasticity of the sample approximately follows the power-law rheological model (Torvik and Bagley, 1984)

$$\mu = \mu_e \left[1 + (i2\pi f \tau)^m\right], \tag{22}$$

with $\mu_e = 49.3$ kPa, $\tau = 3.5 \times 10^{-5}$ s and $m = 0.45$, as shown in Fig. 2(c). The speeds of the SS waves predicted by this model agree quantitatively with our experiments (see Fig. 2(d)). According to the definition given in Eq. (21), the Q for the SS waves (2 kHz to 20 kHz) are less than 3.4. And to make $Q > 6.29$, f_s should be lower than 300 Hz, a frequency that is too low for the OCT system to capture the SS waves even if they exist.

To study the scenario when $Q > 6.29$ with our OCT system, we performed measurements on a piece of hydrogel sample in which entanglements greatly outnumber cross-links. This type of hydrogel has a relatively low material damping, as recently shown by Kim et al. (2021) (details on the sample preparation can be found in this paper). Fig. 4(a) and (b) show the surface waves in the spatial and wavenumber domains, respectively, when the stimulus frequency is 31.6 kHz. The wave attenuation is much weaker comparing with the rubber sample. In the wavenumber domain, both the SS and R waves can be clearly identified, although the R wave is dominant. To evaluate the Q, we measured the phase gradient and attenuation of the R wave using the far field data ($r > 1.2$ mm, see Fig. 4(c) and (d)), where the SS wave has been attenuated. The phase gradient and attenuation give directly the complex wavenumber of the R wave, $k_R = (23.2 - 1.41i)$ mm^{-1}. Therefore, we get $Q \approx 8.23$, well above the restriction 6.29. Certainly, this experiment provides a direct evidence that the SS waves exist without restriction on the quality factor.

5. Acoustoelasticity of supershear surface waves

We proceed to study the effect of prestress on SS waves. To this end, the incremental dynamic theory (Ogden, 2007) is briefly revisited and then adopted to derive the secular equation for the surface waves that incorporates the effect of prestress.

5.1. Incremental dynamics

Consider, a nominal stress $\boldsymbol{N}$ homogeneously deforms the sample from the stress-free configuration to the current configuration in which the surface waves propagate. The infinitesimal elastic wave $\boldsymbol{u}$ in the current configuration is governed by the incremental dynamic equation (Ogden, 2007)

$$\mathcal{A}^0_{piqj}\partial^2 u_j/\partial x_p \partial x_q - \partial \hat{\bar{p}}/\partial x_i = \rho \partial^2 u_i/\partial t^2, \tag{23}$$

where the Einstein summation convention has been adopted. $\boldsymbol{\mathcal{A}}^0$ is the Eulerian elasticity tensor and defined as $\mathcal{A}^0_{piqj} = F_{p\alpha}F_{q\beta}\partial^2 W/\partial F_{i\alpha}\partial F_{j\beta}$ $(i,j,p,q,\alpha,\beta = 1,2,3)$, where $W(\boldsymbol{F})$ is the strain energy function, $F_{i\alpha} = \partial x_i/\partial X_\alpha$ is the deformation gradient, and x_i and X_α denote the Cartesian coordinates of the points in the current and stress-free configurations. The nominal stress is related to the strain energy function by $\boldsymbol{N} = \partial W/\partial \boldsymbol{F} - \bar{p}\boldsymbol{F}^{-1}$, where $\bar{p}$ is the Lagrange multiplier for the incompressibility constraint.

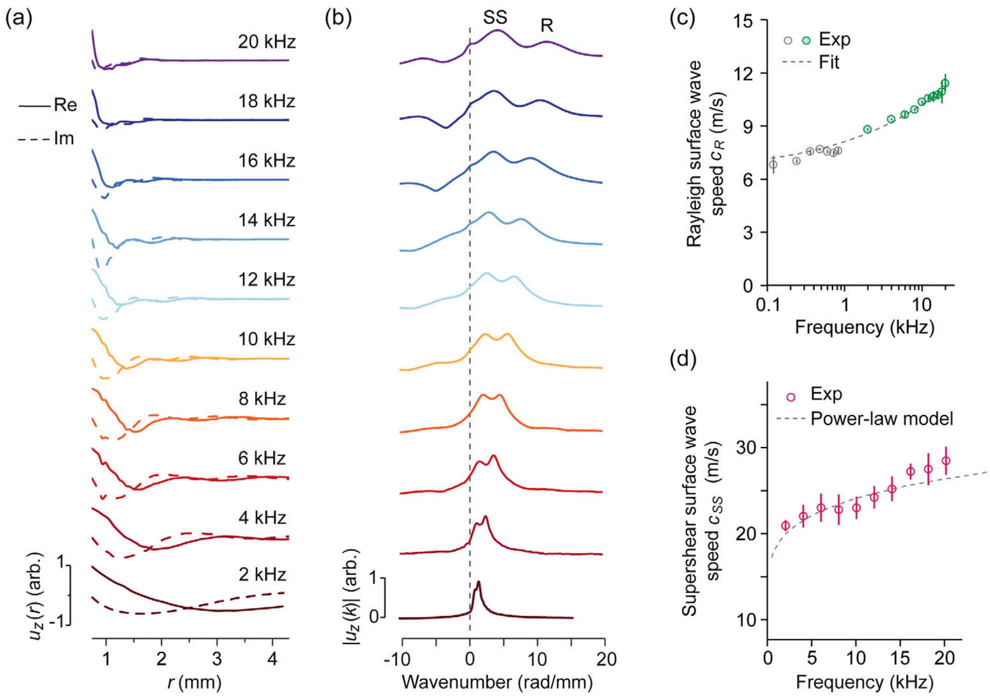

Fig. 2. (a) The real and imagery parts of the surface displacement. (b) The Fourier transformation of the surface displacement to resolve the R and SS waves. (c) Phase velocity of R wave. The low frequency data (gray markers) was obtained using the same experimental setup as the high frequency measurements (green markers). Dashed line, fitting curve using the power-law rheological model with $\mu_e = 49.3$ kPa, $\tau = 3.5 \times 10^{-5}$ s and $m = 0.45$. (d) Phase velocities of the SS wave and the comparison with the power-law model.

$\hat{\bar{p}}$ denotes the increment of $\bar{p}$. Denote the principal stretch ratios by λ_i ($i = 1, 2, 3$), then we have $\boldsymbol{F} = \mathrm{diag}(\lambda_1, \lambda_2, \lambda_3)$. For the incompressible materials we are interested in this study, $\lambda_1\lambda_2\lambda_3 = 1$ and

$$\nabla \cdot \boldsymbol{u} = 0. \tag{24}$$

We consider the plane wave in $x_1 - x_3$ (i.e., $u_2 = 0$ and $\partial()/\partial x_2 = 0$). From Eq. (24) we can introduce a stream function $\chi(x_1, x_3, t)$ such that: $u_1 = \partial\chi/\partial x_3$ and $u_3 = -\partial\chi/\partial x_1$. Inserting these into Eq. (23) and eliminating $\hat{\bar{p}}$ we can get

$$\alpha\chi_{,1111} + 2\beta\chi_{,1133} + \gamma\chi_{,3333} = \rho(\chi_{,11tt} + \chi_{,33tt}), \tag{25}$$

where $()_{,i}$ and $()_{,t}$ denote the partial deviates with respect to coordinate x_i ($i = 1, 3$) and t, and

$$\alpha = \mathcal{A}^0_{1313}, \quad 2\beta = \mathcal{A}^0_{1111} + \mathcal{A}^0_{3333} - 2\mathcal{A}^0_{1133} - 2\mathcal{A}^0_{3113}, \quad \gamma = \mathcal{A}^0_{3131}. \tag{26}$$

5.2. Surface wave

On the surface ($x_3 = 0$) the stress-free boundary conditions apply. So the incremental nominal stresses, denoted by $\hat{\boldsymbol{N}}$, which can be expressed with χ by (Ogden, 2007)

$$\hat{N}_{31} = -\gamma\chi_{,11} + \gamma\chi_{,33}, \quad \hat{N}_{33,1} = \rho\chi_{,3tt} - (2\beta + \gamma)\chi_{,113} - \gamma\chi_{,333}, \tag{27}$$

should be zeros.

To derive the secular equation for surface wave, we can take

$$\chi = \bar{\chi}e^{-skx_3}e^{i(\omega t - kx_1)}, \tag{28}$$

where s is a dimensionless attenuation and $\bar{\chi}$ is a constant amplitude. Substitution of Eq. (28) into Eq. (25) yields

$$\gamma s^4 - (2\beta - \rho C^2)s^2 + \alpha - \rho C^2 = 0, \tag{29}$$

where $C = \omega/k$. Here we use s_1 and s_2 to denote the two roots of Eq. (29) that have positive real parts. Similar as the discussion in Section 3, for Rayleigh surface wave we take

$$\chi = \left(\bar{\chi}_1 e^{-s_1 kx_3} + \bar{\chi}_2 e^{-s_2 kx_3}\right) e^{ik(Ct - x_1)}, \tag{30}$$

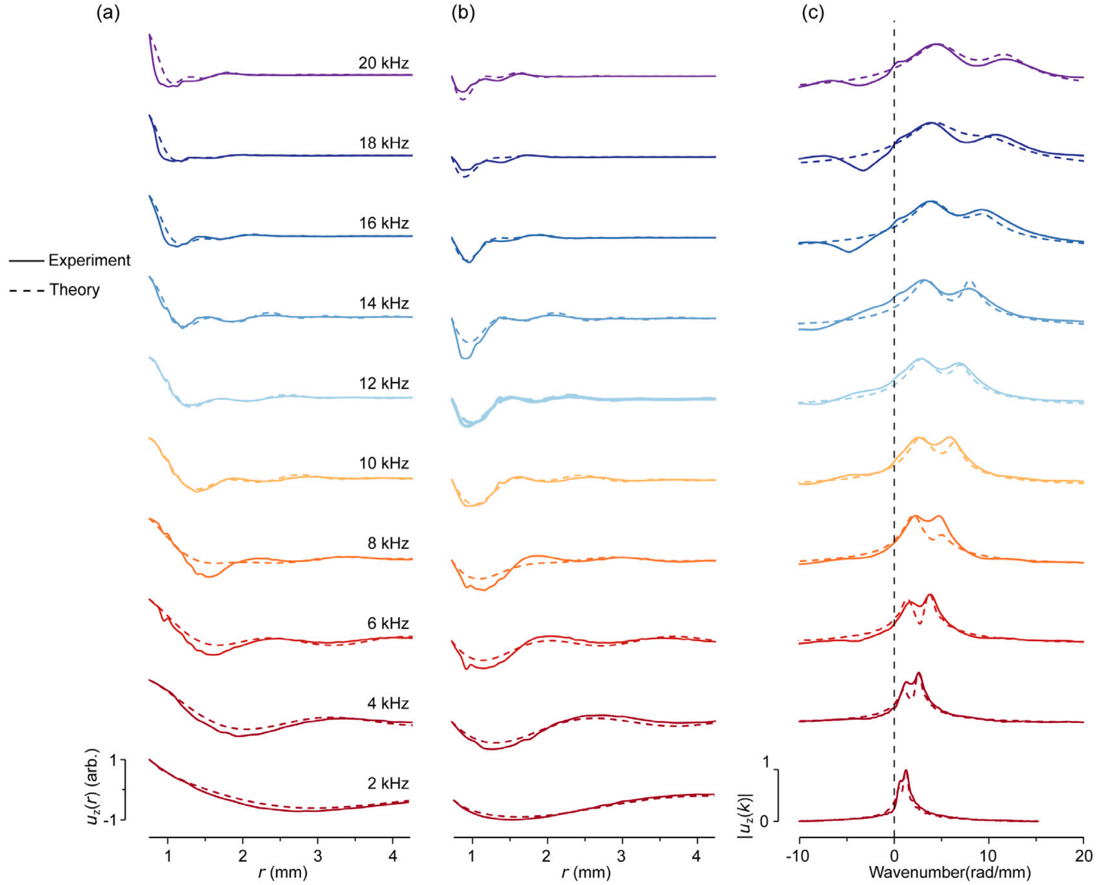

Fig. 3. Comparison between experiment and theory. (a) and (b) Real and imagery parts of the surface displacements. (c) Fourier transformations of the displacements. Solid and dashed lines denote experiment and theory, respectively.

where

$$s_1^2 + s_2^2 = (2\beta - \rho C^2)/\gamma, \quad s_1^2 s_2^2 = (\alpha - \rho C^2)/\gamma \tag{31}$$

according to Eq. (29). Substitution of Eq. (30) into Eq. (27) yields the following linear equations of $\bar{\chi}_1$ and $\bar{\chi}_2$

$$(s_1^2 + 1)\bar{\chi}_1 + (s_2^2 + 1)\bar{\chi}_2 = 0, \quad \left[2\beta + \gamma - \rho C^2 - \gamma s_1^2\right] s_1 \bar{\chi}_1 + \left[2\beta + \gamma - \rho C^2 - \gamma s_2^2\right] s_2 \bar{\chi}_1 = 0. \tag{32}$$

To have nontrivial solutions for Eq. (32) we must have

$$\gamma(\alpha - \gamma - \rho C^2) + (2\beta + 2\gamma - \rho C^2)\left[\gamma(\alpha - \rho C^2)\right]^{\frac{1}{2}} = 0. \tag{33}$$

In the derivation of Eq. (33) we have used Eq. (31).

For the supershear surface wave, we should take, without loss of generality, s_1 and $-s_2$. In this way we get a sign change in Eq. (33). Similar as Eq. (18), we finally get

$$\gamma(\alpha - \gamma - \rho C^2) + (2\beta + 2\gamma - \rho C^2)\left[\gamma(\alpha - \rho C^2)\right]^{\frac{1}{2}} \operatorname{sign}\{\operatorname{Re}(\alpha - \rho C^2)\} = 0. \tag{34}$$

Eq. (34) is the secular equation that incorporates the effect of the prestress, from which the phase velocity of the surface wave c can be obtained by $c = \left[\operatorname{Re}(C^{-1})\right]^{-1}$. While different notations has been adopted, Eq. (34) will reduce to Eq. (18) in the absence of prestress ($\alpha = \beta = \gamma = \mu$, where μ is the linear shear modulus).

It has been shown that the parameters α and β can be directly related to the Cauchy principal stresses (Li et al., 2020). Then for third-order elasticity ($2\beta \approx \alpha+\gamma$), we can infer α and β, and thus the prestress, from the speeds of the two surface waves. Establishing such an inverse method to infer the prestress is an exciting topic, which, however, falls out of the scope of current work.

To demonstrate the effect of the prestress, here we consider a nominal uniaxial stress $\boldsymbol{N}_{11}$ in a lateral coordinate, x_1, and its resulting nominal strain ε along the direction. For isotropic, incompressible, hyperelastic materials, the deformation gradient tensor is given by $\boldsymbol{F} = \operatorname{diag}(1+\varepsilon, (1+\varepsilon)^{-1/2}, (1+\varepsilon)^{-1/2})$. Among different hyperelastic models, we consider the Mooney–Rivlin model that

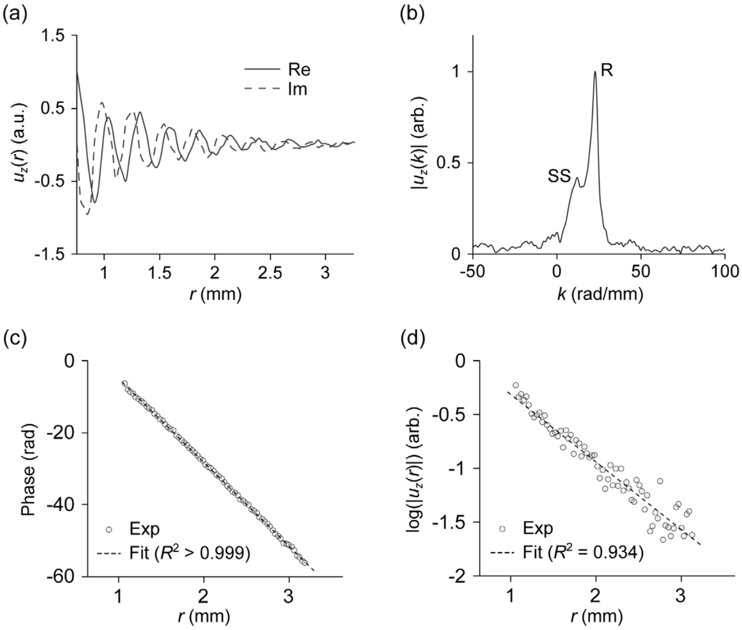

Fig. 4. Surface waves measured in a tough hydrogel (31.6 kHz). (a) Real and imagery parts of the surface displacement. (b) Wave amplitude in the wavenumber domain obtained by the Fourier transform of (a). Amplitude (c) and phase (d) of surface displacement in the far field ($r > 1.2$ mm). The linear fits of (c) and (d) give $k_R = (23.3 - 1.41i)$ mm^{-1}.

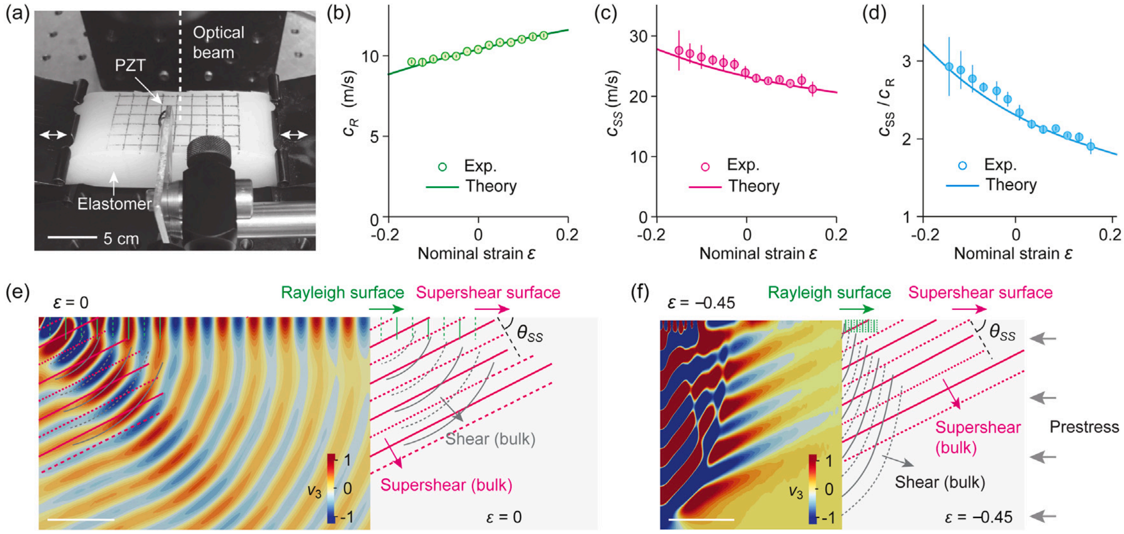

Fig. 5. (a) Uniaxial extension setup. (b)–(c) Variations of the phase velocities of the R and SS waves, and (d) their ratios at different ε. Circles, experimental data measured at f_s = 12 kHz; error bars, standard deviation of five measurements. Solid lines, theoretical solutions with μ = 119 kPa and ζ = 0. (e)–(f) FE simulations of the wave field (left) and illustrations of different waves (right) in a soft material under (e) stress-free and (f) compressive ($\varepsilon = -0.45$) conditions. The solid and dashed lines denote the peaks and valleys of the waves. The intersections of two solid or dashed lines correspond to constructive interference, whereas the intersections of solid and dashed lines correspond to destructive interference. The compressive stress decreases the speed of the Rayleigh surface wave dramatically, making the SS and Rayleigh surface waves separated in space. Please see the supplementary video for the animation of surface wave propagation. θ_{SS} denotes the propagation angle of the SS wave in the medium. Scale bars, 2 mm.

is widely used for rubbery materials under modest deformation ($0 < \varepsilon < 100\%$) (Kim et al., 2011; Destrade et al., 2017). It describes the strain energy function as

$$W(\boldsymbol{F}) = (\mu/2)\left[\zeta\left(I_1 - 3\right) + (1-\zeta)\left(I_2 - 3\right)\right]. \tag{35}$$

Here, μ is shear modulus, ζ is a material-dependent parameter ($0 \le \zeta \le 1$), $I_1 = \mathrm{tr}(\boldsymbol{C})$, and $I_2 = \left[I_1^2 - \mathrm{tr}(\boldsymbol{C}^2)\right]/2$, where $\boldsymbol{C} = \mathrm{tr}(\boldsymbol{F}^{\mathrm{T}}\boldsymbol{F})$. With the strain energy function, the relation between the stress and strain can be derived. For small strain we get

$$N_{11} \approx 3\mu\varepsilon[1-(2-\zeta)\varepsilon]. \tag{36}$$

The instantaneous moduli defined in Eq. (26) are $\alpha = \mu[\zeta(1+\varepsilon)^2 + (1-\zeta)(1+\varepsilon)]$, $\gamma = \mu[\zeta/(1+\varepsilon) + (1-\zeta)/(1+\varepsilon)^2]$, and $\beta = (\alpha+\gamma)/2$. Then we can get the speeds for the R and SS waves by solving Eq. (34). For small ε we obtain the following results:

$$\begin{aligned} c_R &\approx 0.955 c_{T0}\left[1 + (0.5\zeta + 0.644)\varepsilon + (-0.125\zeta^2 + 0.322\zeta - 0.351)\varepsilon^2\right], \\ c_{SS} &\approx 2.13 c_{T0}\left[1 + (0.5\zeta - 0.752)\varepsilon + (-0.125\zeta^2 - 0.376\zeta + 1.03)\varepsilon^2\right], \end{aligned} \tag{37}$$

where $c_{T0} = \sqrt{\mu/\rho}$. For the SS wave, please note C has a nonzero imagery part, $0.567c_{T0}[1+(0.5\zeta-1.36)\varepsilon+(-0.125\zeta^2-0.679\zeta+1.17)\varepsilon^2]$, which characterizes the attenuation along the propagation direction. Note that the coefficient of the linear ε term for the SS wave is always negative for $\zeta = [0,1]$.

Using a custom-built mechanical setup (Fig. 5(a)), we applied different magnitudes of prestress to the sample and measured the surface waves. Fig. 5(b)–(d) shows the experimental results for a range of ε from −0.2 to 0.2. The R wave velocity increases with ε as expected. Interestingly, we find that the SS wave velocity decreases with the strain, the opposite behavior. The best fit to Eq. (37) was obtained with $\zeta \approx 0$. Then the ratio of $c_{SS}/c_R \approx 2.23 - 3.26\varepsilon + 5.31\varepsilon^2$ according to Eq. (37), uniquely related to ε.

To understand the negative sensitivity of c_{SS} to ε, we performed finite element (FE) simulations (Abaqus/standard 6.13, Dassault Systèmes Simulia Corp.). A square domain 40 × 40 mm^2 was built. We checked the height of the model was large enough to avoid wave reflections at the bottom. The left side of the domain was a symmetric boundary and the bottom was completely fixed. In the study of prestress, we used the built-in Mooney–Rivlin model as the material model (μ = 25 kPa, ζ = 1, and $\rho = 10^3$ kg/m^3,). A compression along the horizontal direction was applied on right side of the domain in a static analysis step. In the subsequent analysis we used an implicit dynamic analysis step and applied a time-harmonic, local pressure (0.3 mm) to the surface to excite elastic waves. The wave speed is independent from the frequency because the material is purely elastic. In the simulation the stimulus frequency was 5 kHz. We adopted a gradient mesh (∼ 0.025 mm to ∼ 0.5 mm from top to bottom of the domain) and the CPE8RH element type (8-node biquadratic, reduced integration, hybrid with linear pressure). Convergence of the simulation was confirmed because further reduce the size of the elements did not change the results.

Fig. 5(e) illustrates wave motion in the $x_1 - x_3$ plane in the stress-free configuration. Three distinct waves from the excitation point are seen: the R wave with phase planes normal to the surface, the SS wave with phase planes tilt at a angle θ_{SS}, and a spherical shear wave. The SS wave is a leaky surface wave, whose energy is radiated into the medium in the form of a planar shear wave. This shear wave has a speed of c_{T0}. The leaky angle θ_{SS} satisfies Snell's law (Auld, 1973): $c_{SS}\cos(\theta_{SS}) = c_{T0}$, from which $\theta_{SS} = 62°$. The SS wave can be viewed as a shear wave created at the surface and propagating with the steep angle into the medium. Now, we have a qualitative explanation for the negative dependence of c_{SS} on ε. As the medium is stretched in x_1, it is compressed in x_3 by the Poisson effect. This compression decreases shear wave speeds along x_3, just like compression in x_1 decreases wave speeds along x_1. Since the propagation direction of the SS wave is more vertical than horizontal, the effect of prestress on c_{SS} is opposite to that of c_R.

Fig. 5(f) shows the FE simulation at $\varepsilon = -0.45$. Under uniaxial prestress, the angle-dependence of the shear wave speed can be derived by taking

$$\chi = \bar{\chi} e^{ik(c_T t - x_1\cos\theta - x_3\sin\theta)}, \tag{38}$$

for the stream function, where θ denotes the angle between the wave propagation direction and x_1 axis. Substitution of Eq. (38) into Eq. (25) leads to

$$c_T = \sqrt{(\alpha\cos^4\theta + 2\beta\sin^2\theta\cos^2\theta + \gamma\sin^4\theta)/\rho}. \tag{39}$$

With Eq. (39) and the Snell's law $c_{SS} = c_T(\theta_{SS})\,/\,\cos(\theta_{SS})$, we find the variation of θ_{SS} is $< 1.4°$ over $-0.5 \le \varepsilon \le 0.5$, as shown in Fig. 6. Therefore, $c_{SS} \approx 2.13\, c_T(\theta = 62°, \varepsilon)$. Whereas $c_R \approx 0.955 c_T(\theta = 0°, \varepsilon)$.

6. Supershear surface waves in anisotropic materials

From the angular interpretation discussed above, we expect c_{SS} to be sensitive to material anisotropy, which results from the direction dependence for the shear wave speed. Consider the plane-strain state ($\varepsilon_{22} = 0$) of an incompressible, stress-free linear orthotropic material, of which the material symmetric axes are aligned with the coordinate system shown in Fig. 1(a). The Hooke's law that links the stress and strain is

$$\sigma_{11} = -\bar{p} + C_{11}\varepsilon_{11} + C_{13}\varepsilon_{33}, \quad \sigma_{33} = -\bar{p} + C_{13}\varepsilon_{11} + C_{33}\varepsilon_{33}, \quad \sigma_{13} = C_{55}\varepsilon_{13}, \tag{40}$$

where C_{11}, C_{33}, C_{13}, and C_{55} are components of the orthotropic stiffness matrix (Auld, 1973). $\bar{p}$ is the Lagrange multiplier for incompressibility constraint. According to the third equation we can get the in-plane shear modulus $\mu_{13} := \sigma_{13}/\varepsilon_{13} = C_{55}$. Because of the incompressibility we have $\varepsilon_{33} = -\varepsilon_{11}$. Subtracting the second equation from the first equation and taking $\sigma_{33} = 0$ we get $\sigma_{11} = (C_{11} + C_{33} - 2C_{13})\varepsilon_{11}$ and thus the plane strain Young's modulus $E_1^* := \sigma_{11}/\varepsilon_{11} = (C_{11} + C_{33} - 2C_{13})$. We introduce an anisotropy index $\bar{A} = E_1^*/\mu_{13} - 4$, which reduces to 0 when the material is isotropic.

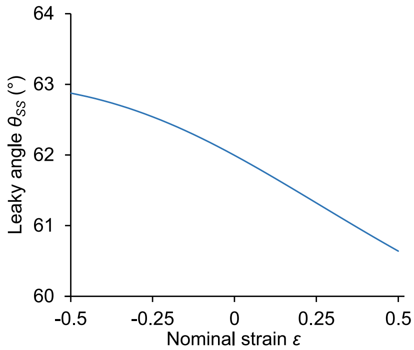

Fig. 6. Effect of prestress on the leaky angle.

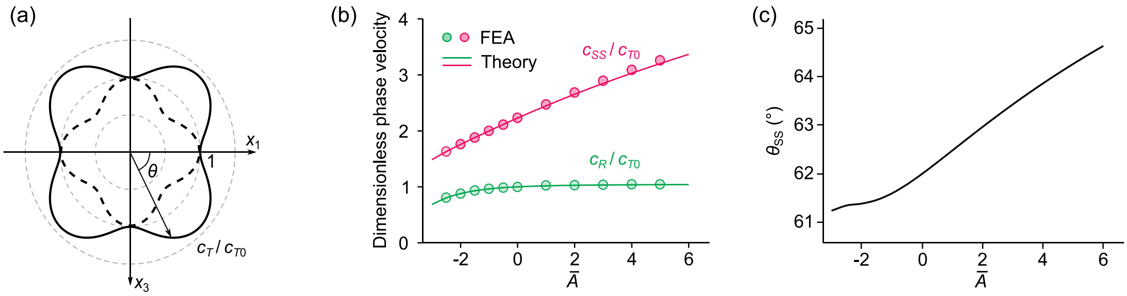

Fig. 7. (a) Normalized phase velocity in an anisotropic material. Solid line, $\bar{A} = 4$, dashed line: $\bar{A} = -2$. (b) The dependence of surface wave speeds on material anisotropy. (c) Variation of the leaky angle θ_{SS} with the material anisotropy.

The surface wave speeds and c_T are given by Eqs. (13) and (39) respectively with $\alpha = \gamma = C_{55}$ and $2\beta = C_{11} + C_{33} - 2C_{13} - 2C_{55}$. The shear wave is isotropic with a speed $c_{T0} = \sqrt{\mu_{13}/\rho}$ when $\bar{A} = 0$ but in general is angle dependent, as shown in Fig. 7(a). While the shear wave speed for $\theta = 0$ remains unchanged, the speeds of the oblique shear waves are sensitive to $\bar{A}$, leading to a much stronger dependence on $\bar{A}$ for the SS wave speed than the R wave speed (see Fig. 7(b)). The FE simulations ($\mu_{13} = 25$ kPa, $\mu_{23} = 9$ kPa and E_1^* varies from 25 kPa to 250 kPa) agree well with the theoretical curves. The leaky angle θ_{SS} has a weak dependence on $\bar{A}$, as shown in Fig. 7(c).

7. Conclusion

In conclusion, we have reported on the properties of the supershear surface wave in soft materials. We provided theoretical and experimental descriptions of the effects of viscoelasticity, prestress and anisotropy of the material on the velocity of the supershear wave. The specific properties of the supershear surface wave are quite distinct from those of the Rayleigh surface waves. The difference gives us an opportunity to use the two wave modes to characterize the material anisotropy or mechanical stress (Li et al., 2020) of bulk materials from measurements at their free surface. One possible application is to characterize soft biological tissues using the two surface waves with OCT elastography (Ramier et al., 2020). The destructive interference of the supershear and Rayleigh surface waves in the near field may be applied to trap and manipulate particle across length scales (Baudoin et al., 2020). Finally, our findings may be useful in the investigations of supershear dynamics of solids, such as ultra-fast dynamic ruptures, where the stress concentration gives rise to the hyperelastic stiffening.

CRediT authorship contribution statement

Guo-Yang Li: Conceptualization, Methodology, Software, Formal analysis, Investigation, Visualization, Writing – original draft. **Xu Feng:** Investigation, Writing – review & editing. **Antoine Ramier:** Conceptualization, Investigation, Writing – review & editing. **Seok-Hyun Yun:** Conceptualization, Supervision, Funding acquisition, Visualization, Writing – review & editing.

Declaration of competing interest

The authors declare that they have no known competing financial interests or personal relationships that could have appeared to influence the work reported in this paper.

Data availability

Data will be made available on request.

Acknowledgment

This study was supported by grants from National Institutes of Health, United States (P41-EB015903, R01-EY027653, DP1-EB024242). The authors thank Dr. Guogao Zhang from John A. Paulson School of Engineering and Applied Science, Harvard University, for providing the hydrogel sample.

Appendix A. Supplementary data

Supplementary material related to this article can be found online at https://doi.org/10.1016/j.jmps.2022.105085.

References

Auld, Bertram Alexander, 1973. Acoustic Fields and Waves in Solids. Wiley, New York.
Barnett, D.M., Lothe, J., 1985. Free surface (Rayleigh) waves in anisotropic elastic half-spaces: the surface impedance method. Proc. R. Soc. Lond. Ser. A Math. Phys. Eng. Sci. 402 (1822), 135–152.
Baudoin, Michael, Thomas, Jean-Louis, Sahely, Roudy Al, Gerbedoen, Jean-Claude, Gong, Zhixiong, Sivery, Aude, Matar, Olivier Bou, Smagin, Nikolay, Favreau, Peter, Vlandas, Alexis, 2020. Spatially selective manipulation of cells with single-beam acoustical tweezers. Nature Commun. 11 (1), 4244.
Bhat, Harsha S., Dmowska, Renata, King, Geoffrey C.P., Klinger, Yann, Rice, James R., 2007. Off-fault damage patterns due to supershear ruptures with application to the 2001 Mw 8.1 kokoxili (kunlun) tibet earthquake. J. Geophys. Res. Solid Earth 112, B06301.
Biryukov, S.V., 1985. Impedance method in the theory of elastic surface-waves. Sov. Phys. Acoust. 31 (5), 350–354.
Carcione, José M., 2007. Wave Fields in Real Media, third ed. Elsevier.
Chadwick, P., Smith, G.D., 1977. Foundations of the theory of surface waves in anisotropic elastic materials. Adv. Appl. Mech. 17 (C), 303–376.
Das, Shamita, 2007. The need to study speed. Science 317 (5840), 905.
Debayle, Eric, Bodin, Thomas, Durand, Stéphanie, Ricard, Yanick, 2020. Seismic evidence for partial melt below tectonic plates. Nature 586 (7830), 555–559.
Destrade, Michel, Saccomandi, Giuseppe, Sgura, Ivonne, 2017. Methodical fitting for mathematical models of rubber-like materials. Proc. R. Soc. Lond. Ser. A Math. Phys. Eng. Sci. 473 (2198), 20160811.
Dong, Erqian, Song, Zhongchang, Zhang, Yu, Ghaffari Mosanenzadeh, Shahrzad, He, Qi, Zhao, Xuanhe, Fang, Nicholas X., 2020. Bioinspired metagel with broadband tunable impedance matching. Sci. Adv. 6 (44), eabb3641.
Farnell, G.W., 1970. Properties of elastic surface waves. In: Mason, Warren P., Thurston, R.N. (Eds.), Physical Acoustics: Principle and Methods. Academic Press, pp. 109–166, Chapter 3.
Friend, James, Yeo, Leslie Y., 2011. Microscale acoustofluidics: Microfluidics driven via acoustics and ultrasonics. Rev. Modern Phys. 83 (2), 647–704.
Fu, Y.B., Mielke, A., 2002. A new identity for the surfaceimpedance matrix and its application to the determination of surface-wave speeds. Proc. R. Soc. Lond. Ser. A Math. Phys. Eng. Sci. 458 (2026), 2523–2543.
Gao, Lingli, Xia, Jianghai, Pan, Yudi, 2014. Misidentification caused by leaky surface wave in high-frequency surface wave method. Geophys. J. Int. 199 (3), 1452–1462.
Garnier, Vincent, Piwakowski, Bogdan, Abraham, Odile, Villain, Géraldine, Payan, Cédric, Chaix, Jean François, 2013. Acoustic techniques for concrete evaluation: Improvements, comparisons and consistency. Constr. Build. Mater. 43, 598–613.
Graff, Karl F., 1991. Wave Motion in Elastic Solids. Dover Publications, New York.
Harris, John G., Achenbach, Jan D., 2002. Comment on ‘‘on the complex conjugate roots of the Rayleigh equation: The leaky surface wave’’ [J. Acoust. Soc. Am. 110, 2867 (2001)] (L). J. Acoust. Soc. Am. 112 (5), 1747–1748.
Herrmann, Jan, Kim, Jin-Yeon, Jacobs, Laurence J., Qu, Jianmin, Littles, Jerrol W., Savage, Michael F., 2006. Assessment of material damage in a nickel-base superalloy using nonlinear Rayleigh surface waves. J. Appl. Phys. 99 (12), 124913.
Kim, Tae Kyung, Kim, Jeong Koo, Jeong, Ok Chan, 2011. Measurement of nonlinear mechanical properties of PDMS elastomer. Microelectron. Eng. 88 (8), 1982–1985, Proceedings of the 36th International Conference on Micro- and Nano-Engineering (MNE).
Kim, Junsoo, Zhang, Guogao, Shi, Meixuanzi, Suo, Zhigang, 2021. Fracture, fatigue, and friction of polymers in which entanglements greatly outnumber cross-links. Science 374 (6564), 212–216.
Le Goff, Anne, Cobelli, Pablo, Lagubeau, Guillaume, 2013. Supershear Rayleigh waves at a soft interface. Phys. Rev. Lett. 110 (23), 236101.
Levshin, A.L., Barmin, M.P., Ritzwoller, M.H., 2018. Tutorial review of seismic surface waves' phenomenology. J. Seismol. 22 (2), 519–537.
Li, Guo-Yang, Gower, Artur L., Destrade, Michel, 2020. An ultrasonic method to measure stress without calibration: The angled shear wave method. J. Acoust. Soc. Am. 148 (6), 3963–3970.
Li, Guo-Yang, Xu, Guoqiang, Zheng, Yang, Cao, Yanping, 2018. Non-leaky modes and bandgaps of surface acoustic waves in wrinkled stiff-film/compliant-substrate bilayers. J. Mech. Phys. Solids 112, 239–252.
Miller, G.F., Pursey, H., Bullard, Edward Crisp, 1954. The field and radiation impedance of mechanical radiators on the free surface of a semi-infinite isotropic solid. Proc. R. Soc. Lond. Ser. A Math. Phys. Eng. Sci. 223 (1155), 521–541.
Munk, Dvir, Katzman, Moshe, Hen, Mirit, Priel, Maayan, Feldberg, Moshe, Sharabani, Tali, Levy, Shahar, Bergman, Arik, Zadok, Avi, 2019. Surface acoustic wave photonic devices in silicon on insulator. Nature Commun. 10 (1), 4214.
Nam, N.T., Merodio, J., Ogden, R.W., Vinh, P.C., 2016. The effect of initial stress on the propagation of surface waves in a layered half-space. Int. J. Solids Struct. 88–89, 88–100.
Nguyen, Thao Thi Phuong, Tanabe-Yamagishi, Rie, Ito, Yoshiro, 2022. Rayleigh wave and super-shear evanescent wave excited by laser-induced shock at a soft solid–liquid interface observed by photoelasticity imaging technique. J. Appl. Phys. 131 (12), 123102.
Norris, A.N., Parnell, W.J., 2012. Hyperelastic cloaking theory: transformation elasticity with pre-stressed solids. Proc. R. Soc. Lond. Ser. A Math. Phys. Eng. Sci. 468 (2146), 2881–2903.
Ogden, Ray W., 2007. Incremental statics and dynamics of pre-stressed elastic materials. In: Destrade, Michel, Saccomandi, Giuseppe (Eds.), Waves in Nonlinear Pre-Stressed Materials. Springer Vienna, Vienna, pp. 1–26.
Ozcelik, Adem, Rufo, Joseph, Guo, Feng, Gu, Yuyang, Li, Peng, Lata, James, Huang, Tony Jun, 2018. Acoustic tweezers for the life sciences. Nature Methods 15 (12), 1021–1028.

Passelègue, François X., Schubnel, Alexandre, Nielsen, Stefan, Bhat, Harsha S., Madariaga, Raù l, 2013. From sub-Rayleigh to supershear ruptures during stick-slip experiments on crustal rocks. Science 340 (6137), 1208.

Pitre, John J., Kirby, Mitchell A., Gao, Liang, Li, David S., Shen, Tueng, Wang, Ruikang K., O'Donnell, Matthew, Pelivanov, Ivan, 2019. Super-shear evanescent waves for non-contact elastography of soft tissues. Appl. Phys. Lett. 115 (8), 083701.

Ramier, Antoine, Eltony, Amira M., Chen, YiTong, Clouser, Fatima, Birkenfeld, Judith S., Watts, Amy, Yun, Seok-Hyun, 2020. In vivo measurement of shear modulus of the human cornea using optical coherence elastography. Sci. Rep. 10 (1), 17366.

Ramier, Antoine, Tavakol, Behrouz, Yun, Seok-Hyun, 2019. Measuring mechanical wave speed, dispersion, and viscoelastic modulus of the cornea using optical coherence elastography. Opt. Express 27 (12), 16635–16649.

Rose, Joseph L., 2014. Ultrasonic Guided Waves in Solid Media. Cambridge University Press, New York.

Royston, T.J., Mansy, H.A., Sandler, R.H., 1999. Excitation and propagation of surface waves on a viscoelastic half-space with application to medical diagnosis. J. Acoust. Soc. Am. 106 (6), 3678–3686.

Rudykh, Stephan, Boyce, Mary C., 2014. Transforming wave propagation in layered media via instability-induced interfacial wrinkling. Phys. Rev. Lett. 112 (3), 034301.

Schröder, Christoph T., Scott, Jr., Waymond R., 2001. On the complex conjugate roots of the Rayleigh equation: The leaky surface wave. J. Acoust. Soc. Am. 110 (6), 2867–2877.

Socquet, Anne, Hollingsworth, James, Pathier, Erwan, Bouchon, Michel, 2019. Evidence of supershear during the 2018 magnitude 7.5 Palu earthquake from space geodesy. Nat. Geosci. 12 (3), 192–199.

Stroh, A.N., 1958. Dislocations and cracks in anisotropic elasticity. Phil. Mag. 3 (30), 625–646.

Stroh, A.N., 1962. Steady state problems in anisotropic elasticity. J. Math. Phys. 41 (1–4), 77–103.

Torvik, P.J., Bagley, R.L., 1984. On the appearance of the fractional derivative in the behavior of real materials. J. Appl. Mech. 51 (2), 294–298.

Walker, Simon V., Kim, Jin-Yeon, Qu, Jianmin, Jacobs, Laurence J., 2012. Fatigue damage evaluation in A36 steel using nonlinear Rayleigh surface waves. NDT E Int. 48, 10–15.

Xu, Feng, Wu, Ke, 2013. Understanding leaky-wave structures: A special form of guided-wave structure. IEEE Microw. Mag. 14 (5), 87–96.

Zhang, Xiaoming, Greenleaf, James F., 2007. Estimation of tissue's elasticity with surface wave speed. J. Acoust. Soc. Am. 122 (5), 2522–2525.